Microvascular Reviews and Communications

©Copyright, 2008, by The JAPANESE SOCIETY FOR MICROCIRCULATION

Vol.2 No.1

Three-dimensional imaging of growing thrombus *in vivo*

Takayuki Morikawa[1)] , Mayumi Kajimura[1),*], Mio Ichikawa[1)] , and Makoto Suematsu[1)]

1) Department of Biochemistry and Integrative Medical Biology, Keio University School of Medicine

Abstract

Although several methods have been developed to investigate thrombus or hemostatic plug formation in microvessels *in vivo*, our knowledge on platelet behavior during such a process is still limited. We, therefore, developed new instrumentation which enables us to induce interactions of individual platelets and to detect their behavior with endothelium in and around the growing thrombus. To evoke a platelet reaction, focal hemorrhage was induced with a nitrogen-dye laser focused through the microscope optics using mesenteric microcirculation of the rat. Platelet deposition at the site of injury was then observed during thrombus formation in real-time. The system was able to provide images with high spatial resolution at video-frame rate that could be used to reconstruct three-dimensional model of a thrombus. (Abstract movie) [MVRC **2**(1): 8-12,2008]

Key Words: thrombus formation, three-dimensional reconstruction, confocal, real-time, intravital microscopy

Received 2007/7/8, Accepted 2007/8/7

To whom correspondence should be addressed: Mayumi Kajimura, Department of Biochemistry and Integrative Medical Biology, Keio University School of Medicine
35 Shinano-machi, Shinjuku-ku, Tokyo160-8582, Japan
TEL: +81-3-3353-1211 (extension 63915) FAX: +81-3-3358-8138
E-mail: myk30@sc.itc.keio.ac.jp

Introduction

Process of thrombus or normal hemostatic plug formation upon vascular injury is initiated by the activation of circulating platelets. Biological and rheological properties of platelets have been extensively studied in the experimental systems *in vitro* such as in a parallel-plate flow chamber. Because platelet responses are affected by many factors in the normal environment, such as endothelium, other circulating cells, and blood flow *per se*, it is inevitable to examine such interactions *in vivo*. In this regard, several methods have been developed to evoke platelet activation and to observe thromboembolic process *in vivo*[1-3] . Among these, the most recent technology was developed by Falti *et al.*[3] with which vascular injury is induced by laser ablation technology and high-speed, near simultaneous acquisition of images of multiple fluorescent probes and the three-dimensional reconstruction of thrombus were made possible. Here we describe a new intravital imaging system that is essentially a modified technique of Falti *et al.*[3]. Because the system utilizes an analog 3CCD camera without using binning function, it was possible to acquire the image in real-time, i.e. 3 x 640 x 480 pixels format, 30 frames s^{-1} which enabled us to evaluate a single platelet behavior *in situ*.

Materials and Methods

Preparation of rats for intravital microscopy

Experiments were approved by the local ethical committee on the use of laboratory animals. Male Wistar rats (250-280 g; Clea Japan, Tokyo) were anesthetized with an intramuscular injection of sodium pentobarbital at 50 mg kg^{-1}, and the femoral vein was cannulated with a polyethylene catheter. Platelets circulating *in vivo* were labeled with an intravenous injection of carboxyfluorescein diacetate succinimidyl ester (CFDA-SE, Morikawa et al. Molecular Probes, Inc., Eugene, OR, USA) as described previously[4,5]. This compound is membrane-permeable and after it has entered cells it is hydrolyzed by esterase which predominantly occurs in platelets and leukocytes. After the dye infusion, the abdomen was opened and the ileocecal portion of the mesentery was arranged on the surface of the glass-coverslip for intravital observation. The mesentery was superfused continuously with the Krebs-Henseleit buffer saturated with 95% N_2/5% CO_2 at 2.0 ml min^{-1} at 37°C.

Thrombus generation by laser ablation of microvascular walls

Either an arteriole or a venule was chosen and endothelial injury was induced by a pulsed nitrogen-dye laser at 440 nm applied through the microscope objective using the MicroPoint laser system . Arterioles with a diameter of 15-30 μm or venules with that of 20-35 μm were targets for the injury.

Intravital imaging of thrombus formation

The imaging system constructed in this study is a modified method of Falati *et al.*[3]. The system was developed around an Olympus BX51W1 up-right microscope with a trinocular head (Olympus, Inc., Tokyo, Japan). Applications of the intravital microscopy in these experiments require either a 40 x (LUMPlanFI/IR, NA 0.8) or a 60 x (LUMFL, NA 1.1) water immersion lens. For confocal microscopy, we used a Yokogawa CSU21 confocal scanner (Yokogawa, Inc., Saitama, Japan) based on Nipkow disk technology. This confocal scanner uses the same pinholes for entrance and exit light beams but is also equipped with a second rotating disk that contains approximately 20,000 pinholes, each with a microlens. The disks rotate together at 1,800 rpm so that the light beams raster-scan the specimen. This technology allows the system to capture up to 360 flashed-frames s^{-1}. An argon-krypton two-line laser (Melles Griot, Carlsbad, CA, USA) provides the fluorescent light for confocal microscopy with excitation at 488 nm and 568 nm. The objective lens was mounted on a piezoelectric driver (Physik Instrumente-PZ73E, PI-Polytec CO., Ltd, Tokyo, Japan) which was controlled by a function generator (SG-4105, Iwatsu, Tokyo, Japan). A schematic representation of the instrumentation is shown in Figure 1.

To generate a laser-induced thrombus, the system was fitted with a nitrogen ablation laser (MicroPoint, Photonic Instruments, St. Charles, IL, USA) which was introduced via the epi-illumination port and was focused on the specimen through the microscope objectives. The output of the laser was at 337 nm but was subsequently tuned through a dye cell. We used coumarin as dye, which emits at 440nm. The laser delivers 4-nsec energy pulses, at a frequency between 3 and 10 Hz, over a surface approximately 1-μm in diameter; the energy of the pulses can be controlled by the operator. In order to conduct consistent ablation, the objective lens was kept at a stationary position until we became certain about a

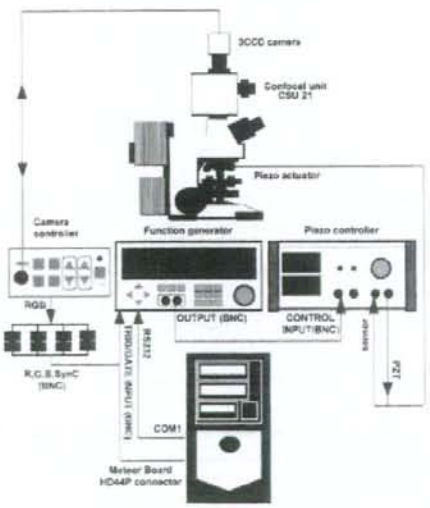

Fig.1 Schematic representation of the experimental setup. See text in Materials and Methods for details.

successful ablation. The ablation was considered successful if erythrocytes left from the vessel, indicating that all components of the vessel layers were damaged. We then started to operate a piezoelectric driver which allows very fine movement in the vertical direction of the sample.

Video acquisition and three-dimensional reconstruction of developing thrombus

The central part of the trinocular stand was connected to an analog color CCD camera (JK-TU52H, Toshiba, Tokyo) that allowed us to record color images with acceptable spatial and temporal resolutions (640 x 480 pixels format, 30 frames s^{-1}). Analog signals were digitized via a frame grabber (Meteor-II, Matrox Electronic Systems Ltd, Tokyo). The computer had a 3 GHz processor, 1 GB of RAM, and three SCSI hard drives including one 160GB-RAID-0. This computer system was capable to acquire real-time color images for the duration of approximately 90 min. Using a piezo-electric driver on an objective lens, optical slices are obtained. Imaging software (StreamPix ver. 3.7.0, Norpix Inc., Montreal, Quebec, Canada) was used to control the hardware components during image acquisition. Finally acquired images were stacked to generate a three-dimensional reconstruction of a developing thrombus by three kinds of imaging software; StreamPix, IP Lab (ver. 3.6.4, Scanalytics, Inc., Fairfax, VA, USA) and Vox Blast (ver. 3.0, VayTek, Inc., Fairfield, Iowa, USA).

Results

Tissue depth of the formed images

Figure 2 shows a representative image of a three-dimensional reconstruction. Here we first positioned the microscope lens at the center of the venule, namely at the point where the largest diameter was seen. The position of the lens was then moved upwards by 22.5 μm and images composed of 640 x 480 pixels with 1.5-μm steps for the total depth of 45 μm were collected. The 45-μm height of the images was intentionally greater than the diameter of the venule in order to compensate for inexact positioning of the lens before the start of the experiment. As seen in Panel A of the x-z section which transverses to the microvessels on this mesentery, only the top half of the circumference of this venule, but not the bottom half of it was visualized. When the dissecting plane was moved 18.7-μm more deeply (Panel B), the shape of the platelet thrombus on this venular wall became apparent. However, when a further 18.3-μm deeper section was made (Panel C), the system failed to form a sharp image. The result suggests a limitation of this optic system as a whole on the tissue depth of image acquisition which was approximately a 30-μm depth from the tissue surface. Therefore microvessels and thrombi residing in the superficial layer lying no more than 30 μm from the surface were subjected to this study.

Thrombus formation upon laser ablation

Upon the injury by laser ablation, a thrombus started to form typically over a 20 second to 1 min period. Thereafter either did it remain rather constant in size

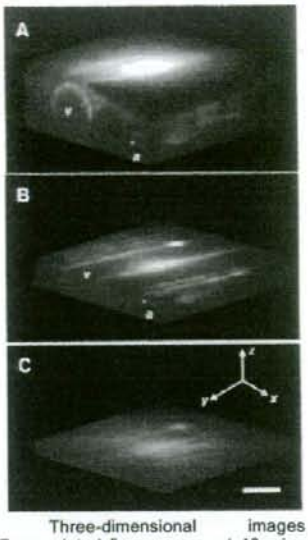

Fig.2 Three-dimensional images of CFSE-associated fluorescence at 10 min after the initial ablation of the venule. At each x-y confocal plane, a 2D image was obtained and these images were stacked in sequential order with an imaging-software to yield a 3D images of the rat mesentery. The image seen in panel A was reconstituted from twenty-eight different x-y planes covered 45-μm depth of the tissue, and each images are 1.5- μm apart. The x-y dissecting plane was moved 18.7-μm (panel B), and further 18.3-μm more deeply (panel C). Scale bar=30 μm. a, arteriole; v, venule.

with producing small emboli or it embolized as a whole cluster and started to form another thrombus. A small population of platelets tethering at the growing thrombus appeared to change their shape from normal discoid to flattened morphology. Figure 3 (Movie 1) shows such a process between 20 seconds and 40 seconds after the start of laser ablation. Spatial distribution of platelets in and around the thrombus was evaluated by three-dimensional reconstruction.

Figure 4 (Movie 2) and Figure 5 (Movie 3) are the representative three-dimensional images where the scan was made on the longitudinal or radial axis of the venule, respectively. As seen, the optical resolution of the system was sufficient to visualize the interaction between the growing thrombus and circulating platelets on this

Fig.3(Movie 1) Developing thrombus upon laser ablation on a venule. Two dimensional images were acquired between 20 seconds and 40 seconds after the start of laser ablation. Towards the end of this movie, the whole thrombus embolized.

Fig.4(Movie 2) Three-dimensional reconstruction of a thrombus induced by laser ablation on a venule. Spatial distribution of platelets in the thrombus was evaluated by this scanning. Scans were made on the x-z plane (vertical) traversing the longitudinal axis of the microvessels. Note that single platelets in the thrombus were visualized.

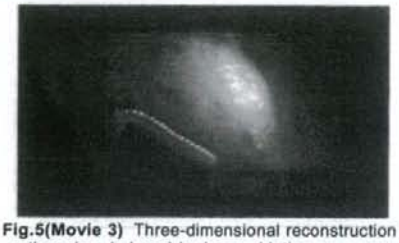

Fig.5(Movie 3) Three-dimensional reconstruction of a thrombus induced by laser ablation on a venule. Spatial distribution of platelets in the thrombus was evaluated by this scanning. Scans were made radially on the x-y plane (horizontal) from the top surface to the approximately the centerline of this venule.

venule.

Figure 6 shows temporal changes in thrombus shape. At 0 second, the initial image showed minimal fluorescence. At 20 seconds, platelets started to accumulate on the point of injury on the vessel wall. At 26 seconds, the platelet thrombus expanded further.

Discussion

In the present study, we established an intravital imaging system with which the platelet interaction can be visualized in real-time during thrombus formation on the mesenteric microcirculation. The optical-and the time-resolution of the system were sufficient to visualize the interaction between the growing thrombus and circulating platelets under the current condition. Utilizing an analog camera system offers the advantage that thrombus formation is visualized on-line with high resolution. This approach therefore enabled us to obtain three-dimensional geometry of the growing thrombus and to study the kinetics of thrombus growth *in vivo*.

To examine the process of thrombus formation, assessment must be ideally performed vertically as well as horizontally through the whole volume of a thrombus. The current system enables to rapidly acquire the information for a thrombus residing in the superficial layer lying no more than 30 μm from the mesenteric surface. It could be speculated that due to the light scattering properties of the imaged tissue, confocal images often suffer from significant intensity attenuation in deeper parts of the specimen[6,7]. The reason could be that both the laser as well as the emitted light are

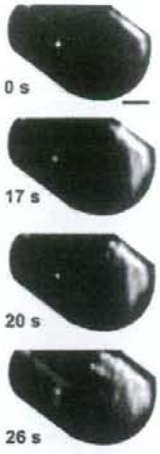

Fig.6 Three-dimensional reconstruction of a growing thrombus showing temporal changes in shape and volume. At each x-y confocal plane, a 2D image was obtained and these images were stacked in sequential order with an imaging-software to yield a 3D image. Representative images of different x-y planes covered 28-μm depth of the tissue, and each images were 1-μm apart. Bar=10 μm.

absorbed and scattered more in deeper parts of the specimen than in parts near the objective lens. This could have caused a greater rejection of the light from the sample to form the image through an array of microlens of Nipkow spinning disk.

Despite the non-ideality of this system discussed above, the system is able to acquire high-spatial resolution images with video-frame rate that can provide us important information to analyze platelet behavior *in vivo*. As seen in Figure 3 (Movie 1), the system is capable of acquiring very sharp images of individual platelets at the site of growing thrombus. Although circulating free flow platelets were rapidly moving, time resolution appears to be appropriate to detect the behavior of tethering and/or adherent platelets of which are the majority in and around a thrombus without severe blur along the longitudinal axis of the vessel (Fig. 4 and 5 (Movie 2 and 3)).

With the laser-induced injury, we observed that as soon as the endothelium was damaged by the laser, platelets rapidly started to accumulate to form a hemostatic plug which was confined at the injured site (Fig. 6). Our methodology allowed us to examine process and content of growing thrombus at the sites of injured vasculature. At present, our system is equipped to capture two different fluorophores that can be excited by 488 nm and 568 nm without crossover of fluorescence. To gain the insight for the kinetics of growing thrombus, its laser source and filter systems should be developed further to visualize the components of growing thrombus other than platelets, e.g. fibrin and tissue factors, which was accomplished by the system of Falati *et al*[3]. In conclusion, the current instrumentation enables us to unravel the biological and rheological properties of single platelet behavior in and around a developing thrombus *in vivo*.

Acknowledgements

This work was supported by Health Labour Sciences Research Grant, Research on Advanced Medical Technology from the Ministry of Health Labour and Welfare (to M.K.), and Grant-in-Aid for Creative Scientific Research, Leading Project for Biosimulation, the 21st Century Center-of-Excellence Program from the Ministry of Education, Culture, Sports, Science and Technology in Japan (to M.S.). Our gratitude goes to Mr. Toshihiro Ochiai who immensely helped us to make this system work.

References

1) Arfors KE., Dhall DP., Engeset J., Hint H., Matheson NA., Tangen O.: Biolaser Endothelial Trauma as a Means of Quantifying Platelet Activity *in vivo*. *Nature*. **218**: 887-888, 1968.
2) oude Egbrink MG., Tangelder GJ., Slaaf DW., Reneman RS.: Thromboembolic reaction following wall puncture in arterioles and venules of the rabbit mesentery. *Thromb Haemost*. **59**: 23-28, 1988.
3) Falati S., Gross P., Merrill-Skoloff G., Furie BC., Furie B.: Real-time *in vivo* imaging of platelets, tissue factor and fibrin during arterial thrombus formation in the mouse. *Nat Med*. **8**: 1175-1180, 2002.
4) Katayama T., Ikeda Y., Handa M., Tamatani T., Sakamoto S., Ito M., Ishimura Y., Suematsu M.: Immunoneutralization of glycoprotein Ibalpha attenuates endotoxin-induced interactions of platelets and leukocytes with rat venular endothelium *in vivo*. *Circ Res*. **86**: 1031-1037, 2000.
5) Suematsu M., DeLano FA., Poole D., Engler RL., Miyasaka M., Zweifach BW., Schmid-Schonbein GW.: Spatial and temporal correlation between leukocyte behavior and cell injury in postischemic rat skeletal muscle microcirculation. *Lab Invest*. **70**: 684-695, 1994.
6) Shen CL., Scott GL., Merchant F., Murphy RM.. Light scattering analysis of fibril growth from the amino-terminal fragment beta(1-28) of beta-amyloid peptide. *Biophys J*. **65**: 2383-2395, 1993.
7) Hell S., Reiner G., Cremer C, Stelzer EHK.: Aberrations in confocal fluorescence microscopy induced by mismatches in refractive index. *J Microscopy*. **169**: 391-405,1993.

Available online at www.sciencedirect.com
ScienceDirect
Colloids and Surfaces A: Physicochem. Eng. Aspects 318 (2008) 184–190
COLLOIDS AND SURFACES A
www.elsevier.com/locate/colsurfa

Fabrication of free-standing nanoparticle-fused nanosheets and their hetero-modification using sacrificial film

Yosuke Okamura[a], Saori Utsunomiya[a], Hidenori Suzuki[b], Daisuke Niwa[c], Tetsuya Osaka[c], Shinji Takeoka[c,*]

[a] *Graduate School of Advanced Science and Engineering, Waseda University, Tokyo 169-8555, Japan*
[b] *Center for Electron Microscopy, The Tokyo Metropolitan Institute of Medical Science, Tokyo 113-8613, Japan*
[c] *Consolidated Research Institute for Advanced Science and Medical Care, Waseda University, Tokyo 169-8555, Japan*

Received 11 September 2007; received in revised form 11 December 2007; accepted 19 December 2007
Available online 6 January 2008

Abstract

Sheet-shaped carriers, having obverse and reverse surfaces and thus a large contact area as a targeting site, have several advantages over spherical-shaped carriers, which have an extremely small contact area. Herein is proposed a novel method for the preparation of free-standing nanoparticle-fused nanosheets having uniform micrometer shape, nanometer thickness and heterogenous surfaces, using a water-soluble sacrificial film. This was achieved by combination of four processes: (1) specific adsorption of latex beads at pH 5.0 and a concentration of 1.0×10^{11} mL^{-1} onto a patterned dodecyltrimethoxysilane self-assembled monolayer (DTS-SAM) region by a conventional dry patterning process, (2) fabrication of the latex bead-sheet via thermal-fusion at 110 °C for 60 s, (3) preparation of the free-standing nanosheet by detachment from the DTS-SAM, and (4) hetero-modification of the resulting nanosheet using a water-soluble poly(acrylic acid) as a sacrificial supporting film. Thus, this sheet-shaped carrier having hetero-surfaces can be regarded as a new material for delivery of drugs, hemostatic reagents and as wound dressings for burn injury, etc.
© 2007 Elsevier B.V. All rights reserved.

Keywords: Free-standing; Nanosheet; Thermal fusion; Sacrificial film; Hetero-modification

1. Introduction

In recent years, much attention has been paid to drug delivery systems (DDS) as a new pharmacological approach for improving the efficacy and safety of drugs. In DDS, vesicles, micelles, emulsions, and biodegradable nanoparticles have been extensively studied as carriers for biologically active substances such as drugs, recognition proteins, enzymes, genes, etc. [1]. There are two concepts for the development of DDS, passive and active targeting systems. In the latter case, recognition proteins such as antibodies and various ligands are conjugated to the surface of the carriers to target tissue epitopes or specific cells.

The present group has developed biocompatible and biodegradable nanoparticles such as albumin-based nanoparticles [2,3] and phospholipid vesicles [4,5] carrying recombinant fragments of platelet membrane proteins [2,4] and fibrinogen dodecapeptide as a recognition site for activated GPIIb/IIIa on the platelet surface [3,5]. These nanoparticles specifically recognize the site of a bleeding injury or activated platelets. In this approach to the conjugation of high or low molecular weight molecules such as glycoprotein Ibα and dodecapeptide to the surface of the particle, it was observed that the activity of the peptide was suppressed by steric hindrance of the large protein; therefore, a spacer such as a poly(ethylene glycol) chain was found to be necessary to conjugate the peptide [6].

On the other hand, sheet-shaped carriers, having obverse and reverse surfaces and thus a large contact area as a targeting site, have several advantages over spherical-shaped carriers, which have a relatively small contact area. Recently, several approaches have been implemented for fabrication of free-standing films, combining a large surface area with

* Corresponding author at: Consolidated Research Institute for Advanced Science and Medical Care, Waseda University, 3-4-1, 65-208 Ohkubo Shinjuku-ku, Tokyo 169-8555, Japan. Tel.: +81 3 5286 3217; fax: +81 3 5286 3217.
E-mail address: takeoka@waseda.jp (S. Takeoka).

0927-7757/$ – see front matter © 2007 Elsevier B.V. All rights reserved.
doi:10.1016/j.colsurfa.2007.12.049

nanoscale thickness. These approaches have included the use of polymers and/or inorganic materials such as cast films [7], layer-by-layer (LbL) films of polyelectrolytes [8–10], cross-linked amphiphilic Langmuir–Blodgett films [11], self-assembled monolayers (SAMs) [12] and assemblies of triblock copolymers [13].

Organosilane SAMs have been widely used in applications designed to change physical and chemical properties of the surface of glass, quartz, SiO_2/Si wafers, or silica particles [14]. Furthermore, they are excellent tools for immobilization of proteins such as redox proteins [15], enzymes [16] and immunogloblins via covalent or non-covalent bond formation; ionic or hydrogen bonding, van der Waals attraction, or hydrophobic interaction occurs with various terminal groups of SAMs. It is generally easy to construct patterned SAMs with uniform size and shape on silicon oxide using conventional photolithography processes [17]. The present group recently proposed a novel method for preparation of free-standing biocompatible nanosheets derived from recombinant human serum albumin (rHSA) molecules adsorbed on patterned hydrophobic SAMs [18].

Two-dimensional patterns with steady repeatability in the particle array have been achieved by site-selective deposition using chemical bonding or electrostatic interaction [19], an electrophotography method [20], a micromold method and gravity [21], a micromold method and a lateral capillary force [22], a patterned Au film and a drying process of colloidal solution onto the patterned Au film [23], an excellent method of HSA-supported lipid patterns by using a micro-contact printing technique to immobilize microspheres and *E. coli* [24,25]. Furthermore, a novel method for deposition of a close-packed particle monolayer onto a patterned hydrophilic SAM was also recently reported using a liquid mold whose drying process was also described [26,27]. However, there is no report on the preparation of free-standing nanoparticle-based nanosheets having uniform micrometer shape, nanometer thickness and heterogenous surfaces, for use as sheet-shaped carriers.

Herein is proposed a novel method for the preparation of a free-standing nanoparticle-based nanosheet with uniform shape and thickness, incorporating hetero-modification of the obverse and reverse surfaces using a poly(acrylic acid) (PAA) film as a sacrificial layer. A patterned hydrophobic dodecyltrimethoxysilane SAM (DTS-SAM) on silicon oxide was used to prepare the nanosheets. Furthermore, latex beads were used as model particles with high monodispersibility, and fluorescent dyes were used to modify the surface of the sheet and to prove the hetero-modification of the nanosheet by staining the sheet surfaces.

2. Materials and methods

2.1. Reagents

P-type Si (100) wafers (below 0.02 Ω cm) covered with thermally grown silicon oxide (approximately 200 nm), were purchased from KST World, Co. (Fukui). *n*-Dodecyltrimethoxysilane (DTS, 97%) was purchased from Gelest, Inc. (Morrisville, PA). Latex beads (Polybead™, Ø100 nm) were purchased from Polysciences, Inc. (Warrington, PA). Fluorescein-4-isothiocyanate (FITC) and 5,(6)-tetramethylrhodamine isothiocyanate (TRITC) were purchased from Dojindo Laboratories, Inc. (Kumamoto) and Invitrogen, Co. (Carlsbad, CA), respectively. Poly(acrylic acid) (Mw = 450,000) and 0.1% (w/v) poly-L-lysine solution were obtained from Sigma–Aldrich Co. (Saint Louis, MO). A microBCA kit was purchased from Pierce Biotechnology, Inc. (Rockford, IL). Recombinant human serum albumin (rHSA, 250 mg mL^{-1}) was kindly donated by Oxgenix Co. Ltd. (Tokyo).

2.2. SAM preparation

Silicon wafers were treated with SPM (96% H_2SO_4:30% H_2O_2 = 4:1 (v/v)) at 120 °C followed by rinsing with distilled water. The resulting wafers were placed in a 20-mL teflon vial containing a glass cup filled with 200 μL DTS liquid. The vials were sealed with a cap and then heated for 8 h at a constant temperature of 110 °C in a dry room to prepare a hydrophobic DTS-SAM on the silicon oxide [28].

2.3. Patterning processes

The patterned DTS-SAM with hydrophobic dodecyl regions and hydrophilic silicon oxide regions on the substrate were prepared by a conventional photolithography process. The DTS-SAM on the silicon oxide was covered with photoresist (OFPR-800 500 cP, Tokyo Ohka Kogyo, Co. Ltd., Kanagawa), and was irradiated with a 350-nm UV lamp (MA-10, Mikasa Ltd., Tokyo) using a photomask (size: 1 cm × 1 cm, patterning; rectangle (5 μm × 10 μm), Topic Co., Ltd., Saitama). After developing (NMD-3), the substrate was exposed to oxygen plasma (Plasma Reactor PR301, Yamato Scientific Co. Ltd., Tokyo) at an input power of 200 W and an oxygen flow rate of 80 sccm for removal of DTS. The photoresist was removed by acetone washing to obtain a patterned DTS-SAM.

2.4. Contact angle measurements

A 3-μL drop of distilled water was placed directly onto the DTS-SAM with a micro-pipette before and after adsorption of latex beads at pH 5.0, or after the addition of surfactant as described below. The liquid drops were observed with an optical microscope with 5× magnification. All water contact angles were represented as the mean ± standard deviation of five measurements.

2.5. Measurement of the glass transition temperature of the latex beads

The glass transition temperature (T_g) of the latex beads was measured by differential scanning calorimetry (DSC, Thermo plus DSC 8230, Rigaku Co., Osaka). The analysis was performed with approximately 10 mg of freeze-dried sample under a dynamic nitrogen atmosphere with a heating rate of 10 °C min^{-1}.

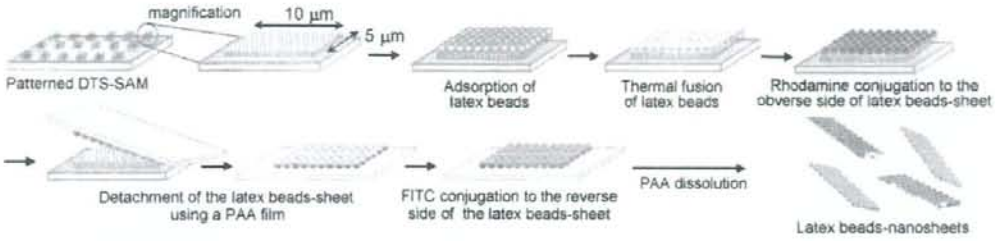

Fig. 1. Preparation of free-standing latex bead-fused sheets having hetero-surfaces using the patterned DTS-SAM.

2.6. Preparation of free-standing latex bead-fused nanosheets

Latex beads (Ø100 nm) were mixed with an rHSA solution (20 mg mL^{-1}) and incubated at r.t. for 2 h to coat the surface of the latex beads with rHSA. After separation of the free rHSA by ultracentrifugation (100,000 × *g*, 10 min, 4 °C, twice), the rHSA-coated latex beads (rHSA-latex beads, 5.0×10^{12} mL^{-1}) were dispersed into a phosphate buffer solution (pH 7.4). The amount of rHSA adsorbed on the surface of the latex beads was analyzed with a microBCA kit.

As shown in Fig. 1, the substrate of the patterned DTS-SAM was immersed in an acetate buffer suspension (pH 5.0) of the rHSA-latex beads at a concentration of 1.0×10^{11} mL^{-1}. After withdrawing the substrate from the suspension, the remaining suspension on the substrate was slowly blown off with a horizontal stream of N_2 in order to adsorb the latex beads onto the hydrophobic dodecyl patterned region, after which the substrate was immediately washed with distilled water. The series of adsorption and washing procedures of latex beads on the substrate was repeated 10 times in order to obtain a closely packed pattern of latex beads. After drying the substrate under a N_2 flow, the substrate was heated at 110 °C for 60 s to thermally fuse the adsorbed latex beads. Poly(acrylic acid) was dissolved in distilled water (20 mg mL^{-1}) to prepare a PAA solution, the PAA cast on the substrate and dried at r.t. for 15 h to make a supporting film. After peeling off the resulting PAA film, it was dissolved in a phosphate buffer solution at pH 7.4 to obtain free-standing latex bead-fused nanosheets. The resulting nanosheets were observed with a Hitachi S-4500 field emission scanning electron microscope (SEM) as follows: the nanosheets adsorbed on a silicon substrate and the free-standing nanosheets collected on the membrane filter (pore size 0.4 μm, Nuclepore®, Whatman, Inc., Clifton, NJ) were coated with osmium tetroxide (ca. 5-nm thick) using an osmium plasma coater (NL-OPC80, Nippon Laser & Electronics Lab., Nagoya), and were observed at an accelerating voltage of 8 kV. In the case of the PAA film, to which the latex bead-fused nanosheets were transferred, the accelerating voltage was set at 1 kV.

2.7. Hetero-modification of the latex bead-fused nanosheets

In this study, a large-scale substrate with the patterned DTS-SAM, established using a photomask (size: 4 cm × 4 cm, patterning; rectangle (5 μm × 10 μm)) was used. As shown in Fig. 1, following thermal treatment the substrate was immersed in a solution of 5-μM TRITC in phosphate buffer (pH 7.4), and incubated at r.t. for 5 min. The unreacted TRITC was removed with distilled water, and the TRITC-labeled nanosheet on the substrate was collected. Next, a PAA solution was cast on the substrate and dried at r.t. for 15 h. After peeling off the PAA film from the substrate, a 5-μM FITC solution in a phthalate buffer (pH 4.0, saturated with sodium chloride) was added to the reverse side of the resulting PAA film to which the TRITC-labeled latex bead-fused sheet had been transferred, and incubated at r.t. for 5 min. Finally, the PAA film was dissolved with a phosphate buffer (pH 7.4) and the fluorescent-labeled nanosheets were then collected and washed with distilled water by centrifugation (1000 × *g*, 5 min, r.t.).

Next, a glass plate (24 mm × 60 mm, thickness 0.12–0.17 mm) was immersed in a poly-L-lysine solution at r.t. for 1 h, and then carefully rinsed with phosphate buffer. The nanosheets was applied to the resulting poly-L-lysine-coated glass plate and incubated at r.t. for 1 h. The resulting nanosheets were observed with a confocal laser scanning microscope (LSM 510, Zeiss, Nikon Co., Tokyo).

3. Results and discussion

3.1. Characterization of the rHSA-latex beads

Latex beads were coated with rHSA molecules to stabilize their dispersion states, to avoid non-specific binding of the latex beads to the substrate, and to be able to conjugate various molecules to the amino groups of rHSA. The quantity of rHSA coating the surface of the latex beads at a concentration of 1.0×10^{11} mL^{-1} was determined to be 14.2 μg mL^{-1} by a microBCA method, from which the number of rHSA molecules on one latex bead (approximate diameter 100 nm) was estimated to be approximately 1.2×10^3 molecules. The theoretical number was calculated to be approximately 1.2×10^3 molecules, assuming that rHSA molecules (the average surface area of one rHSA molecule being 25.5 nm^2) [29] were closely packed on the surface of a latex bead of 100-nm diameter (surface area: 3.1×10^4 nm^2). Consequently, it was possible to estimate the surface of latex beads fully coated with rHSA molecules.

3.2. Water contact angle

The hydrophobic dodecyltrimethoxysilane (DTS), which has a terminal CH_3 group, was selected as a raw material for the

Table 1
Water contact angles of DTS-SAM before and after rHSA-latex beads adsorption

rHSA-latex beads adsorption	Water contact angle (°)
Before	83 ± 1
After	73 ± 3
[a]$C_{12}E_{10}$	82 ± 6

[a] $C_{12}E_{10}$ was added to the DTS-SAM after rHSA-latex beads adsorption and incubated at r.t. for 1 h, and then washed with distilled water.

SAM. The water contact angle of the DTS-SAM-coated substrate was estimated to be 83 ± 1° as shown in Table 1, whereas the contact angle of the silicon oxide surface before DTS coating was estimated to be 20 ± 2°. This supported the conclusion that the hydrophobic DTS-SAM was successfully coated on the silicon oxide surface. When the DTS-SAM-coated substrate was immersed in a dispersion of the rHSA-latex beads in acetate buffer (pH 5.0), the water contact angle was significantly decreased to 73 ± 3°, suggesting that the rHSA-latex beads were adsorbed on the DTS-SAM. When the substrate treated with the rHSA-latex beads was immersed in a 1% (v/v) solution of $C_{12}E_{10}$ for 1 h, the contact angle returned to 82 ± 6° (i.e. the same as that of the DTS-SAM substrate before treatment with the rHSA-latex beads). This indicated that the rHSA-latex beads were adsorbed on the DTS-SAM by hydrophobic interaction and detached by surfactant treatment.

3.3. Specific adsorption of the latex beads and their thermal fusion

A conventional dry patterning process was adopted for the specified adsorption of the rHSA-latex beads onto the patterned DTS-SAM as follows. When the dispersion of the latex beads (1.0×10^{11} mL^{-1}, pH 5.0) was applied to the substrate and the suspension remaining on the substrate was then slowly blown off with a horizontal stream of N_2 gas, the latex beads were arranged as a monolayer on the entire substrate, regardless of hydrophobic and hydrophilic regions (data not shown). It is possible that assembling of the latex beads would involve nucleation initiated by a capillary force and growth driven by a laminar flow to evaporate water; after this the particles might be forced to arrange in the form of a monolayer as previously reported [30].

Next, immediate and repeated washing of the substrate with an acetate buffer (pH 5.0) detached the rHSA-latex beads from the hydrophilic SiO_2 region and beads remained on the rectangular patterns of the hydrophobic dodecyl region only (5 μm × 10 μm). Considering the results obtained from the water contact angle experiment, this indicated that the rHSA-latex beads were firmly adsorbed onto the patterned DTS-SAM by hydrophobic interaction. This would occur because the net charge of the rHSA-latex beads at pH 5.0, near the isoelectric point of rHSA, would be approximately zero. On the other hand, it was assumed that the rHSA-latex beads were easily detached from the SiO_2 region because they were only weakly attracted by hydrophobic interaction with the hydrophilic SiO_2 region (where the ζ-potential of the SiO_2 region at pH 5.0 was extremely negative, ca. −50 mV) [31]. Finally, after repeating the adsorption of the latex beads on the substrate plus washing 10 times, the rHSA-latex beads were closely packed in a monolayer pattern as shown in Fig. 2(A) and (B). On the other hand, at pH 7.4, the rHSA-latex beads were also adsorbed on the entire substrate. After washing, the latex beads were easy to detach from the hydrophilic SiO_2 region and were then scattered on the rectangular patterns of the hydrophobic dodecyl region. This suggested

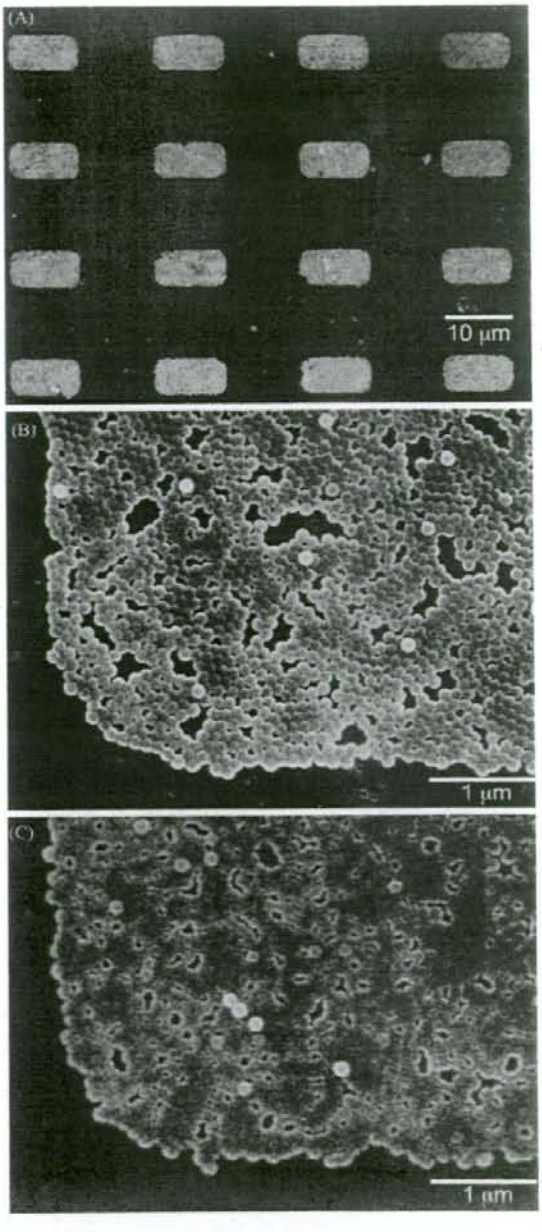

Fig. 2. (A) SEM image of rHSA-latex beads specifically adsorbed onto the patterned DTS-SAM. Magnified SEM image of rHSA-latex beads adsorbed onto the patterned DTS-SAM (B) before and (C) after thermal fusion.

that the rHSA-latex beads, which are negatively charged at pH 7.4, were electrostatically repelled from each other when the particles were arranged by the capillary force of a dry process.

The glass transition temperature of the freeze-dried latex beads was next determined by a DSC measurement in order to thermally fuse the rHSA-latex beads adsorbed on the patterned DTS-SAM; T_g was 109.9 °C. The latex bead-adsorbed substrate was heated at 110 °C for 60 s with a hotplate after drying with N_2. Though the surface of the resulting sheet maintained the spherical configuration of the constituent latex beads, the neighboring latex beads were sufficiently fused under these conditions as shown in Fig. 2(C). When the latex bead-fused nanosheet was detached from the DTS-SAM using a PAA film as described below, it was confirmed that the reverse side of the nanosheet, which was directly adsorbed on the DTS-SAM, was flat and smooth (data not shown). This suggested that it was possible to distinguish the obverse and reverse sides of the nanosheets after detachment. Heating at 110 °C for 30 s, did not yield a sufficiently fused nanosheet. On the other hand, heating for over 120 s resulted in melting and spreading outwards of the latex beads adsorbed on the patterned DTS-SAM (data not shown).

3.4. Preparation of free-standing latex bead-fused nanosheets

PAA was used as a water-soluble sacrificial film to disperse the latex bead-fused sheets. The PAA solution was cast on the substrate where the nanosheets had been adsorbed and dried at r.t. for 15 h. It was easy to peel off the PAA film from the substrate and the resulting film was tough and clear as shown in Fig. 3(A). Observation of the PAA film using an SEM confirmed that the latex bead-fused nanosheet was completely transferred to the PAA film as shown in Fig. 3(B), and no residual sheets were observed on the substrate (data not shown). Such complete transfer is possible because the ionic and/or hydrogen bonding between the PAA and the latex bead-fused nanosheets would be stronger than the van der Waals interaction of the dried nanosheets with the CH_3-terminal SAMs. In agreement with the report by Stroock et al., describing the exquisite transfer of a polymer film on a substrate to a PAA film and suspension in an aqueous buffer, their transfer mechanism has been successfully reproduced in the patterned nanosheets [32]. Furthermore, it was easy to dissolve the resulting PAA film to release the latex bead-fused nanosheet in a phosphate buffer at pH 7.4, and the free-standing nanosheets were collected on the membrane filter as shown in Fig. 3(C). It was confirmed that these nanosheets were able to maintain their rectangular shape, indicating in turn that the neighboring latex beads were sufficiently well fused to retain the two-dimensional shape. Furthermore, it was judged that the thickness of the nanosheets was approximately 100 nm because the latex beads were arranged in a monolayer as shown in Fig. 2(A) and (B).

Detachment of the nanosheets from the substrate was also attempted using other methods. For example, application of sonication for a few minutes caused the latex bead-fused nanosheets to break into pieces although they were dispersed from the substrate. Addition of the surfactant ($C_{12}E_{10}$) was ineffective in detaching nanosheets from the substrate, even by immersion in a 1% $C_{12}E_{10}$ solution for several hours; however, the non-fused latex beads could be simply detached. This suggested that $C_{12}E_{10}$ molecules did not diffuse into the spaces between the nanosheets and the DTS-SAM substrate because (i) the

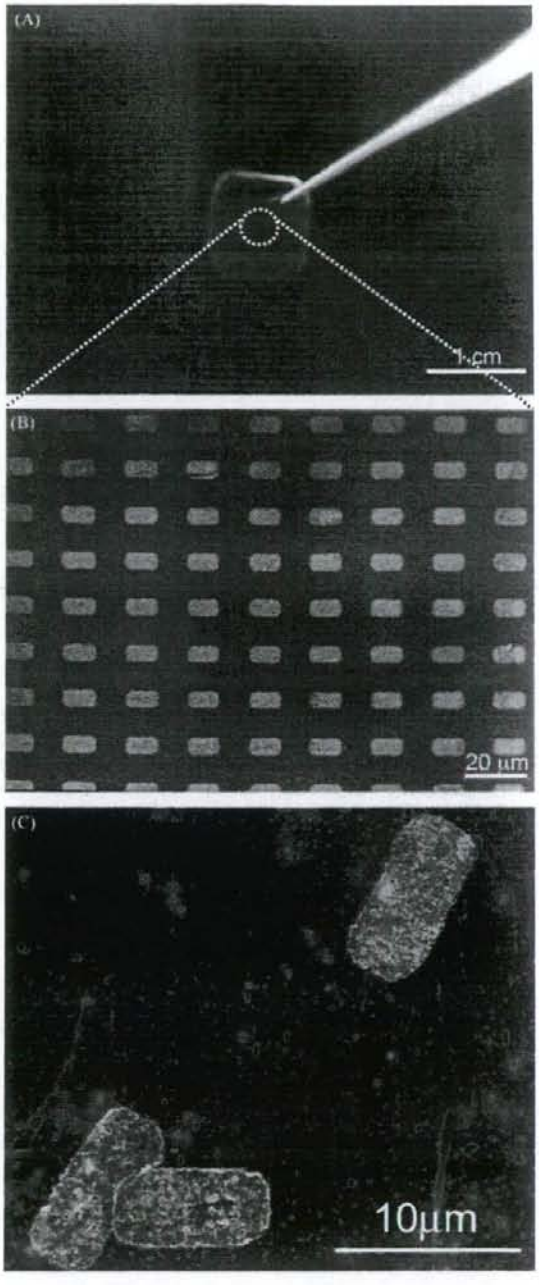

Fig. 3. (A) Photo and (B) SEM image of latex bead-fused nanosheets transferred from the DTS-SAM to the PAA film. (C) SEM image of free-standing latex bead-fused sheets after dissolution of the resulting PAA film.

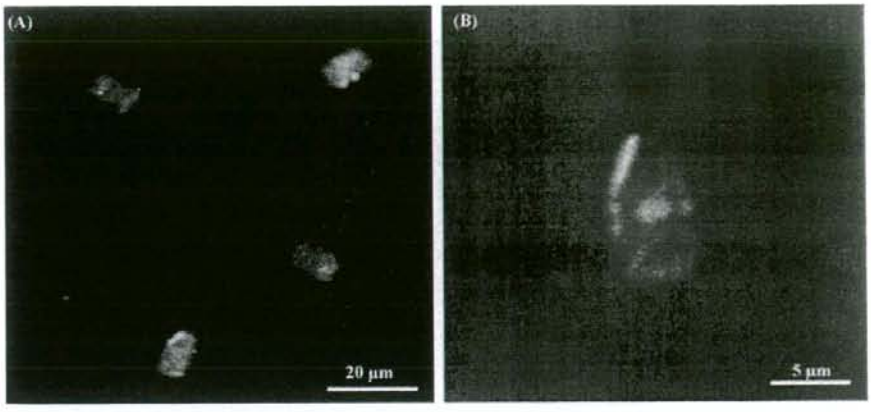

Fig. 4. (A) Images of TRITC and FITC-labeled latex bead-fused sheets and (B) magnified image of the latex bead-fused nanosheets using confocal laser fluorescence microscopy.

nanosheet was interacting two-dimensionally with DTS-SAM and (ii) the hydrophobic bonding of the nanosheet was stronger than that of non-fused latex beads. In summary therefore, it has been confirmed that transference of the nanosheets to the PAA film was an excellent method to achieve dispersion of the nanosheets into an aqueous solution.

3.5. Hetero-modification of the latex bead-fused nanosheet

When the PAA film supporting the latex bead-fused nanosheets was observed, it was easy to confirm that the reverse smooth side of the nanosheet, which had been in direct contact with the silicon substrate, emerged onto the surface of the resulting PAA film (data not shown). It is concluded that either side of the nanosheet could be selectively modified using the PAA film, not only as a tool for transference of the sheets and a sacrificial film for dispersion, but also as a supporting film for hetero-modification of the nanosheet.

Two kinds of water-soluble fluorescent probes, TRITC and FITC were selected as model components to show hetero-modification of the nanosheet. An excess of TRITC (5 μM) was firstly added to the amino groups of the rHSA-adsorbing latex beads on the patterned DTS-SAM. After sufficient washing with distilled water, the PAA solution was cast on the substrate and the dried PAA film was peeled off. For FITC modification of the reverse side of the nanosheets, conditions under which the PAA film would be insoluble were used: pH 4.0 and saturated sodium chloride. An excess of FITC (5 μM) was added to the reverse side of the PAA film which was then dissolved in a phosphate buffer at pH 7.4, to allow collection of latex bead-fused nanosheets coated with each of the two fluorescent labels. Using a confocal laser scanning microscope, the abundance of rectangular nanosheets was confirmed as shown in Fig. 4(A), on one or other of the two surfaces where either fluorescent probe was localized: the obverse side of the nanosheets was conjugated with TRITC and the reverse side was conjugated with FITC (Fig. 4(A) and (B)). Thus, this study has proved that the latex bead-fused sheet was able to modify selectively either surface using the PAA film as a supporting film.

4. Conclusions

Preparation of free-standing rectangular (5 μm × 10 μm) nanoparticle-fused sheets has been successfully achieved by thermal fusion on the patterned DTS-SAM. Also, hetero-modification of the nanosheets on both surfaces has been achieved using the PAA film as a supporting film for hetero-modification. Experimental strategies under development involve preparation of biocompatible and biodegradable free-standing sheet-shaped carriers for drug delivery, delivery of hemostatic reagents and wound dressings for burn injury, etc.

Acknowledgments

This work was supported by 21COE "Practical Nano-Chemistry", "Consolidated Research Institute for Advanced Science and Medical Care" from MEXT, Japan, and Shorai Foundation for Science and Technology (S.T.). Y.O. was the recipient of a Research Fellowships from the Japan Health Science Foundation.

References

[1] Y. Tomii, Lipid formation as a drug carrier for drug delivery, Curr. Pharm. Design 8 (2002) 467–474.
[2] Y. Teramura, Y. Okamura, S. Takeoka, H. Tsuchiyama, H. Narumi, M. Kainoh, M. Handa, Y. Ikeda, E. Tsuchida, Hemostatic effects of polymerized albumin particles bearing rGPIa/IIa in thrombocytopenic mice, Biochem. Biophys. Res. Commun. 306 (2003) 256–260.
[3] Y. Okamura, S. Takeoka, Y. Teramura, Y. Maruyama, E. Tsuchida, M. Handa, Y. Ikeda, Hemostatic effects of fibrinogen γ-chain dodecapeptide-conjugated polymerized albumin particles in vitro and in vivo, Transfusion 45 (2005) 1221–1228.
[4] S. Takeoka, Y. Teramura, Y. Okamura, E. Tsuchida, M. Handa, Y. Ikeda, Rolling properties of rGPIbα-conjugated phospholipid vesicles with different membrane flexibilities on vWf surface under flow conditions, Biochem. Biophys. Res. Commun. 296 (2002) 765–770.
[5] Y. Okamura, I. Maekawa, Y. Teramura, Y. Maruyama, E. Tsuchida, M. Handa, Y. Ikeda, S. Takeoka, Hemostatic effects of phospholipid vesicles carrying fibrinogen γ-chain dodecapeptide in vitro and in vivo, Bioconjug. Chem. 16 (2005) 1589–1596.

[6] Y. Okamura, M. Handa, H. Suzuki, Y. Ikeda, S. Takeoka, New strategy of platelet substitutes for enhancing platelet aggregation at high shear rates: cooperative effects of a mixed system of fibrinogen γ-chain dodecapeptide-or glycoprotein Ibα-conjugated latex beads under flow conditions, J. Artif. Organs 9 (2006) 251–258.
[7] J. Mattson, J.A. Forrest, L. Borjesson, Quantifying glass transition behaviour in ultrathin free-standing polymer films, Phys. Rev. E 62 (2000) 5187–5200.
[8] Z. Tang, N.A. Kotov, S. Magonov, B. Ozturk, Nanostructured artificial nacre, Nat. Mater. 2 (2003) 413–418.
[9] F. Mallwitz, A. Laschewsky, Direct access to stable, freestanding polymer membranes by layer-by-layer assembly of polyelectrolytes, Adv. Mater. 17 (2005) 1296–1299.
[10] A. Mamedov, N. Kotov, Free-standing layer-by-layer assembled films of magnetite nanoparticles, Langumuir 16 (2000) 5530–5533.
[11] F. Mallwitz, W.A. Goedel, Physically cross-linked ultrathin elastomeric membranes, Angew. Chem. Int. Ed. 40 (2001) 2645–2647.
[12] W. Eck, A. Küller, M. Grunze, B. Völkel, A. Gölzhäuser, Freestanding nanosheets from crosslinked biphenyl self-assembled monolayers, Adv. Mater. 17 (2005) 2583–2587.
[13] C. Nardin, M. Winterhalter, W. Meier, Giant free-standing ABA triblock copolymer membranes, Langumuir 16 (2000) 7708–7712.
[14] A. Ulman, An Introduction to Ultrathin Organic Films from Langmuir–Blodgett to Self-assembly, Academic Press, San Diego, CA, 1991.
[15] D.E. Khoshtariya, J. Wei, H. Liu, H. Yue, D.H. Waldeck, Charge-transfer mechanism for cytochrome *c* adsorbed on nanometer thick films. Distinguishing frictional control from conformational gating, J. Am. Chem. Soc. 125 (2003) 7704–7714.
[16] E.E. Ferapontova, S. Shipovskov, L. Gorton, Bioelectrocatalytic detection of theophylline at theophylline oxidase electrodes, Biosens. Bioelectron. 22 (2007) 2508–2511.
[17] D. Niwa, Y. Yamada, T. Homma, T. Osaka, Formation of molecular templates for fabricating on-chip biosensing devices, J. Phys. Chem. B 108 (2004) 3240–3245.
[18] Y. Okamura, T. Goto, D. Niwa, M. Otsuka, N. Motohashi, T. Osaka, S. Takeoka, Fabrication of free-standing albumin-nanosheets having hetero-surfaces, J. Biomed. Mater. Res. A (2008), in press.
[19] Y. Masuda, W.S. Seo, K. Koumoto, Arrangement of nanosized ceramic particles on self-assembled monolayers, Jpn. J. Appl. Phys. 39 (2000) 4596–4600.
[20] H. Fudouzi, M. Kobayashi, M. Egashira, N. Shinya, An arrangement of micrometer-sized powder particles by electron beam drawing, Adv. Powder Technol. 8 (1997) 251–262.
[21] W.J. Wen, N. Wang, D.W. Zheng, C. Chen, K.N. Tu, Two- and three-dimensional arrays of magnetic microspheres, J. Mater. Res. 14 (1999) 1186–1189.
[22] Y. Sun, G.C. Walker, Two-dimensional self-assembly of latex particles in wetting films on patterned polymer, J. Phys. Chem. B 106 (2002) 2217–2223.
[23] Q. Guo, C. Arnoux, R.E. Palmer, Guided assembly of colloidal particles on patterned substrates, Langmuir 17 (2001) 7150–7155.
[24] X. Zhang, Q. He, Y. Cui, L. Duan, J. Li, Human serum albumin supported lipid patterns for the targeted recognition of microspheres coated by membrane based on ss-DNA hybridization, Biochem. Biophys. Res. Commun. 349 (2006) 920–924.
[25] X. Zhang, Q. He, X. Yan, P. Boullanger, J. Li, Glycolipid patterns supported by human serum albumin for *E. coli* recognition, Biochem. Biophys. Res. Commun. 358 (2007) 424–428.
[26] Y. Masuda, K. Tomimoto, K. Koumoto, Two-dimensional self-assembly of spherical particles using a liquid mold and its drying process, Langmuir 19 (2003) 5179–5183.
[27] Y. Masuda, K. Koumoto, Low dimensional particle patterning, J. Disper. Sci. Technol. 25 (2004) 503–511.
[28] H. Sugimura, H. Ushiyama, A. Hozumi, O. Takai, Micropatterning of alkyl- and fluoroalkylsilane self-assembled monolayers using vacuum ultraviolet light, Langmuir 16 (2000) 885–888.
[29] D.C. Carter, J.X. Ho, Structure of serum albumin, Adv. Protein. Chem. 45 (1994) 153–204.
[30] N.D. Denkov, O.D. Velev, P.A. Kralchevsky, I.B. Ivanov, H. Yoshimura, K. Nagayama, Mechanism of formation of two-dimensional crystals from latex particles on substrates, Langmuir 8 (1992) 3183–3190.
[31] A. Hozumi, S. Asakura, A. Fuwa, N. Shirahata, T. Kameyama, Preparation of a well-defined amino-terminated self-assembled monolayer and copper microlines on a polyamide substrate covered with an oxide nanoskin, Langmuir 21 (2005) 8234–8242.
[32] A.D. Stroock, R.S. Kane, M. Weck, S.J. Metallo, G.M. Whitesides, Synthesis of free-standing quasi-two-dimensional polymers, Langmuir 19 (2003) 2466–2472.

Key Interactions in Integrin Ectodomain Responsible for Global Conformational Change Detected by Elastic Network Normal-Mode Analysis

Atsushi Matsumoto,*†‡ Tetsuji Kamata,§ Junichi Takagi,¶ Kenji Iwasaki,‡¶ and Kei Yura*†‡

*Quantum Bioinformatics Team, Center for Computational Science and Engineering, and †Research Unit for Quantum Beam Life Science Initiative, Quantum Beam Science Directorate, Japan Atomic Energy Agency, Kizugawa, Kyoto 619-0215, Japan; ‡CREST, Japan Science and Technology Agency, Kizugawa, Kyoto 619-0215, Japan; §Department of Anatomy, Keio University School of Medicine, Shinjuku, Tokyo 160-8582, Japan; and ¶Institute for Protein Research, Laboratory of Protein Synthesis and Expression, Osaka University, Suita, Osaka 565-0871, Japan

ABSTRACT Integrin, a membrane protein with a huge extracellular domain, participates in cell-cell and cell-extracellular-matrix interactions for metazoan. A group of integrins is known to perform a large-scale structural change when the protein is activated, but the activation mechanism and generality of the conformational change remain to be elucidated. We performed normal-mode analysis of the elastic network model on integrin $\alpha_V\beta_3$ ectodomain in the bent form and identified key residues that influenced molecular motions. Iterative normal-mode calculations demonstrated that the specific nonbonded interactions involving the key residues work as a snap to keep integrin in the bent form. The importance of the key residues for the conformational change was further verified by mutation experiments, in which integrin $\alpha_{IIb}\beta_3$ was used. The conservation pattern of amino acid residues among the integrin family showed that the characteristic pattern of residues seen around these key residues is found in the limited groups of integrin β-chains. This conservation pattern suggests that the molecular mechanism of the conformational change relying on the interactions found in integrin $\alpha_V\beta_3$ is unique to the limited types of integrins.

INTRODUCTION

Integrins are one of the metazoan protein families of adhesion receptors that mediate cell-cell and cell-extracellular-matrix interactions (1). In addition to this function, integrins transmit signals bidirectionally across the plasma membrane. Through these functions, integrins play key roles in diverse biological processes including cell migration, development, immune responses, and vascular hemostasis. They are therefore the target of effective therapeutic drugs against thrombosis and inflammation (1).

Integrin is a heterodimer transmembrane protein complex made of α- and β-chains. In mammals, 18 homologous α-chains and eight homologous β-chains are known so far, and different combinations of α- and β-chains have been identified. Integrins are not constitutively active as receptors. On cell surfaces, integrins are usually in a state of low affinity to their ligands (inactive state). By signals from inside the cell, integrins are supposed to be activated and function as receptors (inside-out signaling) (2).

Solution of the crystal structure of the ectodomain of integrin, $\alpha_V\beta_3$, was a major advance in the study of integrin (3). The crystal structure revealed that the head region was extremely bent over the two nearly parallel tails. Electron microscopy had shown that the integrin had an extended form (4–6), but later, the bent conformation of integrin was also observed. It was then shown that the bent conformation corresponded to the inactive state and the extended conformation to the active state, where integrin has high affinity to its ligand (7). The relationship between two conformations and two functional states is now well demonstrated. However, the transition mechanism between the two conformations is not yet understood.

Here, we studied the conformational changes of integrin ectodomain using normal-mode analysis (NMA) of the elastic network model of the protein. The application of conventional NMA to biomolecules, which employs realistic energy function in contrast to the NMA of the elastic network model, started more than 20 years ago (8–10). Since then, many biomolecules have been studied using NMA. This approach is widely used and has proved very effective for elucidating conformational fluctuations and changes related to biological functions. NMA of the elastic network model of a protein, which is directly related to this work, was first developed by Tirion (11), and the calculated normal modes were shown to faithfully reproduce the B-factors obtained from x-ray crystal structure analysis (12). It requires much fewer computational resources compared to the conventional

Submitted February 5, 2008, and accepted for publication May 6, 2008.

Address reprint requests to Atsushi Matsumoto, Quantum Bioinformatics Team, Center for Computational Science and Engineering, Japan Atomic Energy Agency, 8-1 Umemidai, Kizugawa, Kyoto 619-0215, Japan. Tel.: 81-774-71-3463; Fax: 81-774-71-3460; E-mail: matsumoto.atsushi@jaea.go.jp.

Kei Yura's present address is The Graduate School of Humanities and Sciences, Ochanomizu Univeristy, 2-1-1 Otsuka, Bunkyo, Tokyo 112-8610, Japan.

This is an Open Access article distributed under the terms of the Creative Commons-Attribution Noncommercial License (http://creativecommons.org/licenses/by-nc/2.0/), which permits unrestricted noncommercial use, distribution, and reproduction in any medium, provided the original work is properly cited.

Editor: Peter Tieleman.

© 2008 by the Biophysical Society

0006-3495/08/09/2895/14 $2.00

doi: 10.1529/biophysj.108.131045

method, so that the applications to huge macromolecular structures such as ribosomes and virus capsids (13–17) are possible. Here we applied the NMA of the elastic network model to the ectodomain of integrin $\alpha_V\beta_3$ in the bent form (inactive state). The analysis enabled us to identify the key residues that work as a switch for conformational changes of the integrin ectodomain. Iterative normal-mode calculations demonstrated that the key residues work as a snap to keep the structure in the bent form. The importance of the residues was further verified experimentally.

MATERIALS AND METHODS

Naming scheme for extracellular domains of integrin $\alpha_V\beta_3$

In this article, we follow the widely used naming scheme for the ectodomain of integrin $\alpha_V\beta_3$ (see Xiong et al. (3), for example). The α-chain consists of β-propeller (residues 1–438), thigh (439–592), calf-1 (602–738), and calf-2 (739–956) domains. The β-chain consists of PSI (1–54), hybrid (55–108 and 353–432), βA (109–352), EGF-1 and -2 (453–529), EGF-3 (532–562), EGF-4 (563–605), and βTD (606–690) domains. The PSI and EGF-1 and -2 domains are missing in the x-ray crystal structure to which we applied NMAs.

Elastic network model

In the usual treatment of an elastic network model (12,18), each residue in a protein is represented by the C_α atom. If the distance between two C_α atoms is less than the arbitrary chosen cutoff length, R_c (8–12 Å), the two residues are considered to be neighbors and the two C_α atoms are connected by a spring whose equilibrium length is the same as the distance in the initial conformation. Thus, the distance between the two C_α atoms is considered to be the distance between the two residues. The same spring constant C is used for all springs in the network model.

In this study, we defined the distance between two residues in a different way for the reason explained in the Results and Discussion section. We first considered all atoms except for hydrogens, and calculated the distances between all pairs of atoms. The shortest distance between atoms in two different residues was defined as the distance between the two residues, and if it was less than the arbitrary chosen cutoff length, r_c (3–5 Å), the two residues were considered to be neighbors. Once the neighbors were identified, each residue was represented by the C_α atom, and the C_α atoms in the neighbor residues were connected by springs with an arbitrarily chosen spring constant, C. The adjacent C_α atoms along the amino acid chain were automatically connected by this approach. We further introduced springs along the amino acid chain between C_α atoms in nth and $(n + 2)$th residues and between those in nth and $(n + 3)$th residues. The former spring restrained the fluctuations of the virtual bond angle formed by C_α atoms in nth, $(n + 1)$th and $(n + 2)$th residues, and the latter spring those of the virtual dihedral angle formed by C_α atoms in nth, $(n + 1)$th, $(n + 2)$th and $(n + 3)$th residues.

Normal-mode analysis of the elastic network model

The basic formulation of the NMA of the elastic network model is the same as that for the NMA performed with different coordinate systems and force fields (19–27);

The conformational potential energy of the system is approximated by the multidimensional parabola,

$$V = \frac{1}{2}\sum_{ij} f_{ij}\Delta q_i \Delta q_j, \tag{1}$$

where Δq_i is the instantaneous fluctuation of the ith generalized coordinate q_i from its equilibrium value and f_{ij} is an element of a Hessian matrix, $\mathbf{F}$. The approximation is valid in the vicinity of minimum energy points.

The kinetic energy K is similarly expressed in quadratic form in terms of $\dot{q}_i$, the first derivative of q_i with respect to time, and coefficient h_{ij}, which is an element of the "mass" matrix, $\mathbf{H}$:

$$K = \frac{1}{2}\sum_{ij} h_{ij}\Delta\dot{q}_i \Delta\dot{q}_j, \tag{2}$$

If the Δq_i and $\Delta\dot{q}_i$ are collected in the vectors $\Delta\mathbf{q}$ and $\Delta\dot{\mathbf{q}}$, respectively, Lagrange's equation of motion is simplified to

$$\mathbf{H}\Delta\ddot{\mathbf{q}} + \mathbf{F}\Delta\mathbf{q} = \mathbf{0}, \tag{3}$$

with a solution of the form

$$\Delta q_i = \sum_{n=1}^{N} A_{in}\alpha_n \cos(\omega_n t + \delta_n), \tag{4}$$

where N is the number of freedom in the system. The constant α_n and phase angle δ_n are determined from the initial conditions. The coefficient A_{in} is an element of a matrix $\mathbf{A}$ which simultaneously diagonalizes $\mathbf{H}$ and $\mathbf{F}$; that is, $\mathbf{A}^T\mathbf{H}\mathbf{A} = \mathbf{I}$ and $\mathbf{A}^T\mathbf{F}\mathbf{A} = \mathbf{\Lambda}$, where $\mathbf{A}^T$ denotes the transposition of $\mathbf{A}$, $\mathbf{I}$ is an identity matrix, and Λ is a diagonal matrix with elements $\Lambda_{nn} = \omega_n^2$.

In this study, the conformational potential energy of the elastic network model is expressed in the following form, as was done by Tirion (11):

$$V = \frac{1}{2}\sum_{(a,b)} C(|\mathbf{r}_{ab}| - |\mathbf{r}_{ab}^0|)^2, \tag{5}$$

where C is the spring constant, $\mathbf{r}_{ab}(= \mathbf{r}_b - \mathbf{r}_a)$ is the vector pointing from atom a to atom b, and the superscript zero indicates the initial conformation. Thus, the initial conformation has the minimum energy so that the energy minimization process is not necessary. In our treatment, each residue is represented by a C_α atom, and $\mathbf{r}_a$ and $\mathbf{r}_b$ are regarded as the positions of residues a and b, respectively. The summation is taken over all pairs of the neighboring residues.

If Eq. 5 is expanded about $\Delta\mathbf{r}_{ab}(= \mathbf{r}_{ab} - \mathbf{r}_{ab}^0)$ and terms higher than second order are ignored, it is simplified to

$$V = \frac{1}{2}\sum_{(a,b)} C\left(\frac{\mathbf{r}_{ab}^0 \cdot \Delta\mathbf{r}_{ab}}{|\mathbf{r}_{ab}^0|}\right)^2, \tag{6}$$

from which the Hessian matrix, $\mathbf{F}$, is easily derived. We report the normalized normal-mode frequencies in the Results and Discussion section, because the normal-mode frequencies, which are obtained by diagonalizing the matrix $\mathbf{F}$, are proportional to the square root of the arbitrarily chosen spring constant, C. Our system is described by the Cartesian coordinate, and thus the mass matrix $\mathbf{H}$ is a diagonal matrix with the $(3n - 2)$th, $(3n - 1)$th, and $3n$th diagonal elements equal to the total mass of the nth residue.

Comparison of thermal atomic fluctuations

To see how well the calculated values agreed with experimental values, the correlation coefficient was calculated using the equation

$$cc = \frac{\sum_{i=1}^{n}(x_i - \bar{x})(y_i - \bar{y})}{\sqrt{\sum_{i=1}^{n}(x_i - \bar{x})^2}\sqrt{\sum_{i=1}^{n}(y_i - \bar{y})^2}}, \tag{7}$$

where $\bar{x}$ is the average of x_i. In this study, the correlation coefficient between the thermal atomic fluctuations derived from the NMA and those derived

from the B-factors of the crystal structure was calculated. In the NMA, the thermal atomic fluctuations are given as a sum of contributions from all normal modes except for the six zero-frequency normal modes corresponding to the rigid body motions as a whole. The thermal atomic fluctuations of the crystal structure are proportional to the square root of the B-factors.

Similarity of two normal modes

We studied the effect of interactions between neighboring residues on the molecular motions to detect the key residues for the conformational changes of integrin. For this purpose, we compared low-frequency normal modes calculated for a model with full interactions to those for a model without specific interactions. The comparison of the two normal modes was made in terms of similarity, defined as

$$C_s = \left| \sum_k \mathbf{u}_k^i \cdot \mathbf{v}_k^j \right|, \quad (8)$$

where $\mathbf{u}_k^i$ and $\mathbf{v}_k^j$ are displacement vectors of the k th atom in the i th and j th normal modes, respectively, for the two elastic network models. Here, displacement vectors were normalized as

$$\sum_k \mathbf{u}_k^i \cdot \mathbf{u}_k^i = \sum_k \mathbf{v}_k^j \cdot \mathbf{v}_k^j = 1. \quad (9)$$

If the value is close to 1, the two normal modes are similar to each other. If it is close to zero, they are dissimilar.

Iterative normal-mode calculations

For the conventional NMA, a time-consuming energy minimization process is necessary before the NMA. For the NMA of the elastic network model, the energy minimization process is not necessary, and the NMA can be applied to any given conformation (28). If atoms in a protein are moved by a small amount from the initial positions along the displacement vectors in a normal mode, a slightly different new structure is generated. If the NMA of the elastic network model is applied to this new structure, another new structure can be obtained. By repeating this process, a series of structures is generated. This approach is often used for building atomic models based on electron microscopy density maps (29–31). Here, we call this series of calculations "iterative normal-mode calculation" and use this approach for forcing the conformational change of integrin from the bent to the extended forms and studying the role of the specific interactions in the conformational change.

The x-ray crystal structure of integrin (Protein Data Bank ID 1jv2 (3)) was used as the initial structure (the 0 th structure). After the nth NMA for the $(n-1)$th structure, many structures were generated by deforming the $(n-1)$th structure along each of the three lowest-frequency normal modes, and the structure with the largest distance between the head region and C-terminal end was chosen as the nth structure. The distance was measured between two C_α atoms in the residues Lys^{82} and Glu^{765} of the α-chain. The deformation was restricted so that the root mean-square displacement (rmsd) of the n th structure from the $(n-1)$th is <0.1 Å. The iterative calculation was terminated when the increment of distance between the head and C-terminal end of a new conformation (nth conformation) and that of the previous conformation was <0.1 Å.

Each time a new structure made of C_α atoms was generated by the approach described above, the coordinates of other atoms, which were necessary for updating the network formation, were determined by rigid-body treatment and a least-square fitting procedure (32) as follows. A structure made of a C_α atom in each residue (kth residue) and a few C_α atoms in the nearby residues along the amino acid chain in the x-ray crystal structure was treated as a rigid body and was fitted into the corresponding structure in the newly generated structure by rotational and translational manipulation in the least-square fitting procedure. The same manipulation was then applied to the other atoms in the kth residue of the x-ray crystal structure to get the positions of these atoms in the new structure. This process was repeated for all residues and the coordinates of all atoms in the new structure were obtained.

The purpose of the iterative normal-mode calculation in this study was to clarify the role of specific interactions in the conformational change from the bent to the extended form, in other words, to check whether the specific interactions obstructed the conformational change or not. For this purpose, two different iterative calculations were necessary. In one calculation, the specific interactions were kept, and in the other, they were not. However, the connectivity for the specific interactions could have changed during the iterative normal-mode calculation, because the network formation was to be updated each time a new structure was generated. To avoid this, we did not update the connectivity for the specific interactions during the iteration.

Multiple sequence alignment and conservation pattern of the residues

Homologous amino acid sequences to integrin from *Homo sapiens* $\alpha_V\beta_3$ were searched for out of all the amino acid sequences in UniProt (33) and all the translated amino acid sequences in DDBJ (34) by BLAST (35) with default parameters. Sequences derived from pseudogenes and partial sequences were eliminated. Identical sequences in the obtained set of sequences were grouped and only one of the sequences in each group was kept for building multiple sequence alignment. The multiple sequence alignment was built based on the progressive alignment method (36) using the BLOSUM62 matrix (37). Alignment at regions with extremely low sequence identity was manually adjusted based on the heuristic knowledge that cysteine residues should be well conserved and aligned among homologous extracellular domains. Sequences were grouped into clusters based on a phylogenetic tree built by the neighbor-joining method (38), with evolutionary distances calculated by the method of Kimura (39). The threshold for grouping the integrin sequences was set to be consistent with the annotation of sequences based on a previous study (1). Conservation of amino acid residues at positions of concern in each group was manually identified.

Mutation experiment to verify the activation mechanism

We experimentally verified the activation mechanism of integrin predicted by the NMA. We used integrin $\alpha_{IIb}\beta_3$ instead of $\alpha_V\beta_3$ for mutation experiments. Although the former is exclusively expressed on platelets and megakaryocytes different from the latter, and is known to use a different mechanism of signaling at the cytoplasmic domain of the α-chain (40), it has a common β_3-chain and binds to common ligands such as fibrinogen, fibronectin, and vitronectin in an RGD-dependent fashion. In addition to these structural and functional similarities, it has been well established that $\alpha_{IIb}\beta_3$ increases its affinity for fibrinogen by undergoing structural rearrangement upon inside-out signaling (41). Thus, we took advantage of the $\alpha_{IIb}\beta_3$-fibrinogen interactions to examine the effect of the mutations.

Normal mouse IgG was purchased from Sigma-Aldrich (St. Louis, MO). Anti-α_{IIb} monoclonal antibody (mAb) PL98DF6 (42) was a generous gift from Drs. J. Ylänne (University of Oulu, Oulu, Finland) and I. Virtanen (University of Helsinki, Helsinki, Finland). Anti-$\alpha_{IIb}\beta_3$-complex-specific activating mAb PT25-2 has previously been characterized (43). RPE-conjugated goat antimouse polyclonal antibody was purchased from Biosource (Camarillo, CA). The synthetic peptide Gly-Arg-Gly-Asp-Ser (GRGDS) was purchased from Peptide Research Institute (Osaka, Japan). Fluorescein-isothiocyanate (FITC) was purchased from Sigma-Aldrich. Human fibrinogen (Fbg) was purchased from Experimental Cell Research (South Bend, IN).

The full-length cDNAs for integrin α_{IIb} and β_3 subunits, generous gifts from Dr. Joseph C. Loftus (Mayo Clinic, Scottsdale, AZ), were cloned into the mammalian expression vector pBJ-1, kindly provided by Dr. Mark Davis (University of California, San Francisco, CA). The cDNAs for β_3 mutant L375A, L389A, R404A, R633A, R633del, R404A/R633A, R404A/R633del, and R404A/S674A were created by site-directed mutagenesis us-

ing the Transformer Site-Directed Mutagenesis Kit (BD Biosciences, San Jose, CA).

Chinese hamster ovary (CHO-K1) cells were cultured in Dulbecco's modified Eagle's medium (Invitrogen, Carlsbad, CA) supplemented with 10% fetal calf serum (Hyclone, Logan, UT), 1% penicillin and streptomycin (Invitrogen), and 1% nonessential amino acids (Sigma-Aldrich), and maintained at 37°C in a humidified incubator supplemented with 5% CO_2. Fifty micrograms of α_{IIb} cDNA construct was cotransfected with 50 μg of β_3 cDNA construct into CHO-K1 cells by electroporation. After 48 h, cells were detached and used for assays.

FITC-labeling of human Fbg is described in detail elsewhere (44). In brief, after adjusting the pH of human Fbg at 1 mg/ml in phosphate-buffered saline to 8.5 with 5% Na_2CO_3, 1/100 volume of 10 mg/ml FITC in dimethylsulfoxide was added and incubated at room temperature for 10 min. FITC-labeled Fbg was separated from free FITC on a PD-10 column (Amersham Biosciences, Uppsala, Sweden) equilibrated with HEPES-buffered saline (10 mM Hepes, 150 mM NaCl, pH 7.4). The concentration and *F/P* ratio of FITC-labeled Fbg were calculated as previously described (44). Forty-eight hours after transfection, cells were detached with phosphate-buffered saline containing 3.5 mM EDTA and incubated with nonfunctional anti-α_{IIb} mAb PL98DF6 followed by an RPE-conjugated F(ab')2 fragment of goat anti-mouse IgG. After washing, cells were incubated with FITC-labeled Fbg at 350 μg/ml with or without 1 mM GRGDS peptide in modified HEPES-Tyrode buffer (5 mM Hepes, 5 mM glucose, 0.2 mg/ml bovine serum albumin, and 1× Tyrode's solution) containing 1 mM $CaCl_2$ and 1 mM $MgCl_2$ for 2 h at 4°C. In some experiments, mAb PT25-2 was included at 10 μg/ml to activate $\alpha_{IIb}\beta_3$. After washing, fluorescence was measured on FACS Calibur. The median Fbg binding (FL1) to cell populations expressing high α_{IIb} (FL2 > 500) was calculated. Background binding in the presence of 1 mM GRGDS peptide was subtracted to obtain specific binding. Normalized Fbg binding was calculated by dividing the specific binding by the mean $\alpha_{IIb}\beta_3$ expression (FL2) of the gated population.

RESULTS AND DISCUSSION

Elastic network model of integrin $\alpha_V\beta_3$

The first step of the calculation is the formation of the elastic network model based on the x-ray crystal structure of integrin with a specific cutoff length. Motions of residues in this model depend on the number of neighboring residues. Residues with a small number of neighbors can move with less restraint compared to those with many neighbors. The number of the springs in molecules, which connect the C_α atoms in neighboring residues, depends on the cutoff length. Thus, the cutoff length is the most important parameter determining molecular motions.

As described in Materials and Methods, our definition of the distance between two residues is different from that in the conventional approach. Fig. 1 demonstrates the difference between the two approaches with a specific example. Two residue pairs in integrin, Gly^{172} and Ser^{225} in the α-chain, and Tyr^{274} in the α-chain and Leu^{258} in the β-chain, are shown in Fig. 1 *a* and *b*, respectively. The distances between the two C_α atoms (*black*) are 7.5 Å in both cases, whereas the shortest interatomic distances between the two residues in Fig. 1, *a* and *b*, are 7.0 and 3.3 Å, respectively. In the conventional approach, the two C_α atoms are connected by springs in both cases (assuming $R_c > 7.5$), whereas in our approach the C_α atoms in the former case are not connected and those in the latter case are connected (assuming $3.3 < r_c < 7.0$). Thus, the network formation is more sensitive to the local conformation in our approach.

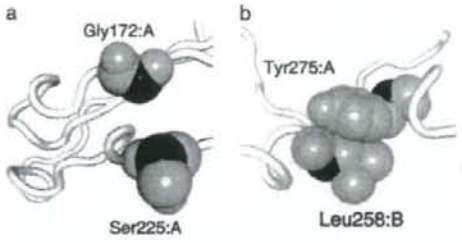

FIGURE 1 Two pairs of residues, Gly^{172} and Ser^{225} in the α-chain (*a*), and Tyr^{274} in the α-chain and Leu^{258} in the β-chain (*b*) in the x-ray crystal structure of integrin demonstrate the difference between the two approaches used to generate an elastic network model. The C_α atoms are colored in black, other atoms in gray. The backbone is represented by a white tube. In the conventional approach, the two residues in both cases are connected by a spring when the cutoff length, R_c, is >7.5 Å. In our approach, the residues in *b* are connected, whereas those in *a* are not, when the cutoff length, r_c, satisfies $3.3 < r_c < 7.0$.

A relatively large number of the pairs of residues are similar to the case shown in Fig. 1 *a*, that is, pairs of residues that have short C_α distances but long interatomic distances. For example, there are 774 pairs of residues in integrin in which the distances between the C_α atoms are between 7.5 and 8 Å, and these are usually regarded as neighboring residues according to the conventional approach. For 197 of these pairs of residues (25%), the shortest interatomic distances are >6 Å, and for 412 pairs (53%), the distances are >5 Å, which means that according to our approach, a fairly large number of the pairs of residues are not regarded as neighboring residues.

In this article, we studied the global conformational change of integrin from the bent to the extended conformation. Before we used our modified approach, we had used the conventional approach to build the elastic network model of the x-ray crystal structure of integrin with normal cutoff length ($R_c = 8$ Å) and had studied the molecular motions. However, we had not observed the motions that could direct the bent conformation of integrin to the extended one in the lowest-frequency normal modes. Some springs between residues must have hindered such motions. Thus, these springs should have been eliminated to promote the conformational change. We therefore tried to remove such springs from the elastic network model. However, it was not easy to find all such springs by eliminating springs one by one and checking the effect by NMA, because multiple springs could have been involved in the hindrance. Instead, we decreased the cutoff length so that springs representing interactions with longer distances would be eliminated, assuming that these interactions would be weaker and less important for the conformational change. To make this assumption more valid, we defined the distance between two residues as the shortest

interatomic distance, as described above. We will discuss the effect of the different definition later.

Dependence of molecular motions on cutoff length, r_c

NMAs were carried out for the elastic network models with various cutoff lengths, and the correlation coefficients were calculated based on Eq. 7. In Fig. 2, the calculated coefficients are plotted against the cutoff length as open circles connected by a solid line. The coefficients for cutoff lengths $>\sim 3.6$ Å were roughly constant. However, at around $r_c =$ 3.2–3.3 Å, the coefficients dropped abruptly. This cutoff length is roughly equivalent to the hydrogen bond distance, suggesting that the springs representing hydrogen bonds were on the verge of elimination in this range of cutoff lengths. A large correlation coefficient suggests that the molecular motions derived from the calculation are similar to those in the crystal structure, whereas a small coefficient suggests molecular motions that are different. We checked that the small coefficients did not stem from extremely large thermal atomic fluctuations, which are often observed for atoms with a small number of neighbors (data not shown).

The change of the molecular motions reflects the change of the energy landscape of the molecule, that is, the energy required for the conformational change from the x-ray crystal structure (bent structure) to the other conformations is altered. Thus, the conformational change to the extended one may become easier.

To identify the interactions that contributed to the sudden change of the coefficient, we eliminated the springs one by one by reducing the cutoff length starting from 3.3 Å, and NMA was performed. There were 231 springs that were to be eliminated when the cutoff length was reduced from 3.3 to 3.2 Å. We found the maximum drop in the coefficient when the spring connecting C_α atoms in Leu^{389} and Arg^{633} in the

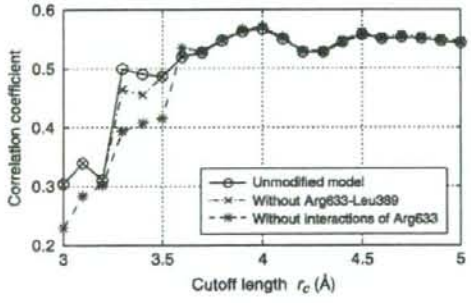

FIGURE 2 Correlation coefficient of the thermal atomic fluctuations derived from NMA and x-ray crystal structural data (B-factor) plotted against the cutoff length. Open circles connected by solid line: unmodified model. "X" symbols connected by dash-dotted line: model without interaction between Arg^{633} and Leu^{389}. Asterisks connected by dashed line: model without interactions between Arg^{633} and nearby nonbonded residues.

β-chain was eliminated, suggesting that the interaction represented by this spring has a large influence on the molecular motions.

The maximum drop in the coefficient observed when the interaction between Leu^{389} and Arg^{633} was eliminated does not mean that the drastic change in molecular motions would be caused by the elimination of the interaction at any cutoff length. If the longer cutoff length were assumed, other interactions would have had to be eliminated at the same time for the drastic change of the coefficient to occur. Thus, this result only suggests that the interaction between Leu^{389} and Arg^{633} was the one with the shortest distance that contributed to keeping the molecular motions as in the x-ray crystal structure. Indeed, the effect of eliminating the interaction between Leu^{389} and Arg^{633} independent of the cutoff length was limited, as shown in Fig. 2, where the correlation coefficients for the network models without the interaction between Leu^{389} and Arg^{633}, irrespective of the cutoff length, are plotted by "X" symbols connected by a dash-dotted line. We found that the effect was enhanced if the interactions of Arg^{633} with other nearby residues were simultaneously eliminated. In Fig. 2, the correlation coefficients are plotted by asterisks connected by a dashed line for the network models in which the C_α atom of Arg^{633} was not connected to the C_α atoms in the nearby nonbonded residues (including Leu^{389}) by springs. In the latter network models, the correlation coefficients were further deviated from those for the original models with full interactions (*open circles*) in the wider range of cutoff lengths. This suggests that the interactions of Arg^{633} with nearby residues have an influence on the molecular motions.

Change of lowest-frequency normal modes of integrin

The above analysis showed that the correlation coefficients dropped when the interactions of Arg^{633} were eliminated. However, it did not tell whether the drop was related to the biologically important conformational change of integrin, that is, the conformational change from the bent to the extended form. In this and the following subsections, we reveal what changed when the correlation coefficient dropped.

The change of the correlation coefficient is due to the change of the normal modes. To see what changed in the normal modes when the correlation coefficient dropped, we compared the lowest-frequency normal modes, which influence the global molecular motions, of the two elastic network models with different correlation coefficients.

The comparison was made for the two network models with and without the springs connecting the C_α atom of Arg^{633} to those in the nonbonded neighboring residues at the cutoff length of 3.4 Å (we call the former model A and the latter model B). At this cutoff length, the molecular motions of model A were similar to those in the x-ray crystal structure (Fig. 2, *open circles*), and by removing the springs of Arg^{633},

quite a large change in correlation coefficient was observed (*asterisks*), indicating that the springs were working as a switch for molecular motions.

A comparison of the five lowest-frequency normal modes for models A and B is shown in Table 1. It is clear that the second-, fourth-, and fifth-lowest-frequency normal modes of model B were similar to the first, second, and third modes of model A, respectively. The normal-mode frequencies were relatively close to each other. However, the first and the third modes of model B were not so similar to any of the five modes of model A. This result indicates that the new types of motions emerged once the interactions of Arg^{633} with other residues were eliminated.

The motion described by the lowest-frequency mode of model B is shown in Fig. 3 *a*. During this motion, the distance between the hybrid domain (Fig. 3, *deep green*; see also Figs. 4 and 8 *a*) and EGF-3 and EGF-4 (Fig. 3, *cyan*; see also Figs. 4 and 8 *a*) oscillated. Due to the springs from Arg^{633}, which connected the βTD (*cyan*; see also Figs. 4 and 8 *a*) with the hybrid domain near the head region (drawn beneath the hybrid domain in Fig. 3), the motions of the hybrid domain of model A were restrained, whereas those in model B were not. In this way, eliminating the interactions of Arg^{633} enhanced separation (opening motions) of the hybrid domain from the EGF domains. This opening motion might further induce elimination of the interactions between the hybrid domain and the EGF domains, which is shown to be important for the conformational change of integrin, as explained later.

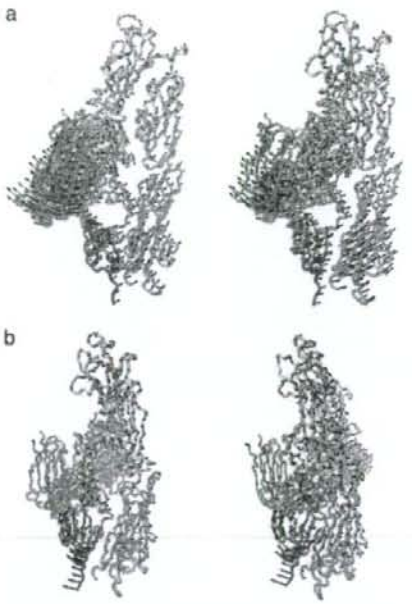

FIGURE 3 Displacement vectors of C_α atoms of integrin in the lowest- (*a*) and third-lowest- (*b*) frequency normal modes of model B (see text) drawn in stereo with the backbone. Leu^{375}, Leu^{389}, and Arg^{633} are shown by a space-filling model. The images were generated with a VMD program (62).

Role of inside-out signaling to local conformational change

Fig. 4 shows the local conformation around Arg^{633} (*cyan*) in the x-ray crystal structure. The residue Arg^{633} belongs to the βTD, and its side chain interacts with residues in the hybrid domain near the head region; the side chain of Arg^{633} is sandwiched by two leucine residues, Leu^{375} and Leu^{389} (*orange*), in the hybrid domain (see also Fig. 8 *b*). Our calculation suggests that the interactions of Arg^{633} with nearby residues influences the molecular motions. If the side chain of Arg^{633} is moved from the position in the x-ray crystal structure to a position where it is no longer sandwiched by the two residues, the interactions of Arg^{633} with nearby residues will be eliminated. Such a motion of the side chain of Arg^{633} was observed only in the third-lowest-frequency mode of the network model-B, as is shown in Fig. 3 *b*. This mode involved the motion of the βTD as a whole. Some external forces should be applied to move βTD and eliminate the interactions of Arg^{633}, to switch model A into model B.

TABLE 1 Comparison of the lowest-frequency normal modes of elastic network models A and B

		Model B				
	Frequency	0.72	0.73	1.36	1.66	2.01
Model A	1.00	0.25	**0.95**	0.02	0.01	0.14
	1.52	0.51	0.11	0.20	**0.82**	0.07
	1.99	0.41	0.00	0.32	0.26	**0.78**
	2.28	0.45	0.14	0.15	0.28	0.52
	2.58	0.32	0.10	0.56	0.35	0.04

Numbers >0.75 are shown in bold. The normal-mode frequencies are shown as relative values with respect to the lowest frequency of model A.

The x-ray crystal structure we used for NMA lacks the cytoplasmic domains and the transmembrane (TM) domains. Although the 3D structure of these domains is not so clear, there are abundant data indicating that the cytoplasmic domains can regulate integrin activation (45–53). These data show that integrin is activated if the membrane-proximal regions of the α and β cytoplasmic tails are separated, and that the interactions between these segments restrain the integrin in an inactive state. These studies were mainly performed on integrin $\alpha_{IIb}\beta_3$. The conformational rearrangement in the cytoplasmic domains should be transmitted to the ectodomains through the TM domains. However, little is known about the role of the TM domains in this process. Similar to the case of the cytoplasmic domains, modification of the membrane-proximal regions of ectodomain to inhibit the separation of the α- and β-chains restrains the activation, whereas enhancing the separation promotes activation (6,7,54).

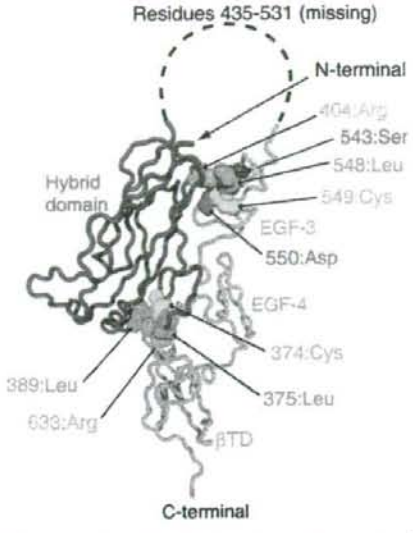

FIGURE 4 Three-dimensional structure of integrin β_3-chain. Arg^{633} and Arg^{404}, with their nearby residues, are shown by a space-filling model.

This experimental evidence is consistent with our results. Separation of the membrane-proximal regions of the α and β cytoplasmic tails, caused by binding of proteins such as talin (55–57), will cause rearrangement of the TM domains. This rearrangement will cause the conformational rearrangement of the βTD, which is close to the TM domain. If the rearrangement is similar to that shown in Fig. 3 *b*, the interactions of Arg^{633} with nearby residues will be eliminated, and the conformational change of ectodomain will be promoted. It is interesting to note that the motions shown in Fig. 3 *b* involve separation of the membrane-proximal regions of the α- and β-chains of the ectodomain, which has been shown to be important for integrin activation (6,7,54).

In Fig. 4, most of the residues involved in the interactions between the hybrid domain and the EGF domains are also indicated by the space-filling model. The amino acid residues that participate in the interactions are the same types as those in the interactions between the βTD and the hybrid domain, and in a similar way; a leucine (*orange*) and a cysteine (*yellow*) are adjacent to each other and in contact with the side chain of an arginine (*cyan*), which connects the two different domains. Compared to Arg^{633}, Arg^{404} is relatively exposed, and the area participating in the interactions is smaller.

Role of local interactions on the global conformational change

We deformed the x-ray crystal structure of integrin by iterative normal-mode calculations and studied the impact of eliminating the interactions we found above on the global conformational change from the bent to the extended forms. To clarify the set of interactions, we named the interactions between Arg^{633} and nearby residues "interaction A", and those between the hybrid domain and the EGF domains "interaction B". We performed four types of iterative normal-mode calculations, namely calculation with both A and B, calculation with A and without B, calculation without A and with B, and calculation without either A or B (Table 2). In all calculations, the cutoff length was set to 3.4 Å.

There are 25 disulfide bonds in the x-ray crystal structure of integrin. These bonds should not have broken during the iterative calculation. Thus, we kept the 25 springs between the residues that were covalently connected by the S-S bond.

In the x-ray crystal structure, residues between Asp^{434} and Lys^{532} in the β-chain were missing. During the iterative calculation, the distance between the two residues could become unrealistically long due to the lack of these residues. To prevent this happening, we added a spring between the C_α atoms in Asp^{434} and Lys^{532} whose spring constant was 1/10 that of the normal spring, assuming that the distance between the two residues was easier to change than those between nearby residues.

Two springs were eliminated in the four iterative calculations to enhance the conformational change. They were the spring between Val^{332} and Ser^{674} in the β-chain and that between Ser^{305} in the α-chain and Arg^{563} in the β-chain. These springs prevented the conformational changes when they were maintained in the calculations. The prevention of the conformational change by the former spring agrees with an experimental result, where the bent conformation was shown to be stabilized if the two residues (Val^{332} and Ser^{674}) were replaced by cysteines and a disulfide bond was formed (7). Even if the two residues were mutated so that they did not interact with each other, however, the ligand-binding affinity of integrin was not perturbed (T. Kamata, M. Handa, Y. Ikeda, and S. Aiso, unpublished data). Thus, the interactions did not play an active role in conformational change. Furthermore, even when the spring between Val^{332} and Ser^{674} was eliminated from the elastic network model for the x-ray crystal structure, new types of global motions, such as those observed when the springs of Arg^{633} were eliminated, did not emerge in the lowest-frequency range. These experimental and computational results suggest that the interactions be-

TABLE 2 Summary of four iterative normal-mode calculations

Calculation No.	Interaction A	Interaction B	Final conformation
1	–	–	Extended
2	–	+	L-shaped
3	+	–	Bent
4	+	+	Bent

Interaction A refers to the interactions of Arg^{633} with Cys^{374}, Gly^{388}, and Leu^{389}, and interaction B to those of Arg^{404} with Ser^{543}, Leu^{548}, Cys^{549}, and Asp^{550} plus the interactions between Glu^{364} and Ser^{551}. The plus and minus symbols mean that the springs representing these interactions exist or do not exist, respectively.

tween Val^{332} and Ser^{674} need to be eliminated for the conformational change of integrin, but that the elimination does not have the effect of enhancing the conformational change. The spring between Ser^{305} in the α-chain and Arg^{563} in the β-chain was eliminated for similar reasons. An experiment to replace a loop region in the α_{IIb}-chain, which corresponds to the loop including Ser^{305} in the α_V-chain, with that in the α_5-chain suggested that the interactions between Ser^{305} and Arg^{563} do not have an influence on the conformational change (58). Iterative normal-mode calculations showed that the spring needed to be eliminated for the conformational change. However, eliminating the spring from the elastic network model for the x-ray crystal structure had little effect on the lowest-frequency normal modes.

Among the four iterative calculations, integrin fully extended in one case, when the springs for both interactions A and B were eliminated (Fig. 5 *a*, and Table 2, *calculation 1*). In calculation 2 of Table 2, the conformational change terminated when the molecule took on an L-shape, as shown in Fig. 5 *b*. This result demonstrated the importance of eliminating interaction B for the conformational change to the fully extended form. The results of calculations 3 and 4 (Fig. 5, *c* and *d*) were quite similar. The corresponding structures (nth structures) during the iterative calculations were also similar to each other (rmsd < 3 Å). This result suggests that eliminating interaction B has a small effect on the conformational change if interaction A is maintained. The four iterative calculations clearly demonstrated that interaction A (interactions involving Arg^{633}) works as a snap to keep integrin in the bent form.

Comparison with the conventional elastic network model

Our elastic network model differs from the conventional model in the definition of the distance between two residues. We introduced this definition so that the network formation would be more sensitive to the local conformation, as described earlier. Here, to observe the effect of the difference in definition, we carried out the same calculations as those performed to obtain Fig. 2 using the conventional elastic network model. Decreasing the cutoff length tends to destabilize the elastic network model. To avoid this, we modified the conventional elastic network model by introducing springs, irrespective of the cutoff length, along the amino acid chain between C_α atoms in the nth and $(n + 2)$th residues and between those in nth and $(n + 3)$th residues, which is the same procedure as in our elastic network model. The calculated correlation coefficients are plotted against cutoff length R_c in Fig. 6. The coefficients were relatively large and roughly constant when the cutoff length, R_c, was >7.8 Å, indicating that the molecular motions derived from the calculations were similar to those in the crystal structure. In our elastic network model, the coefficient took similar values when the cutoff length, r_c, was >3.3 Å, as shown in Fig. 2. There were 8332 springs in the conventional model with $R_c =$ 7.8 Å, and 5512 springs in our elastic network model with $r_c = 3.3$ Å. The two network models had 5342 springs in common. Thus, the conventional model had 2990 additional springs and our model had 170 additional springs. The former springs correspond to the case shown in Fig. 1 *a*, but the latter do not correspond to any cases in Fig. 1. In the interactions represented by the latter case, amino acid residues with long side chains, such as Tyr or Arg, were often involved. The correlation coefficient between the thermal atomic fluctuations from the B-factors and those from the elastic network model, which was made from the common 5342 springs, was low (0.28). Thus, these additional springs were necessary in both models to reproduce the molecular motions in the crystal structure. However, there were obviously many more additional springs in the conventional model, suggesting that there were many springs in the conventional model that were not critically important for reproducing the molecular motions in the crystal structure.

Fig. 6 shows that the coefficient decreased noticeably as the cutoff length became shorter than 7.8 Å. However, the decrease was gradual compared to Fig. 2. In Fig. 2, the coefficient decreased by ~0.2 when the cutoff length was changed from 3.3 to 3.2 Å, whereas in this case, the same

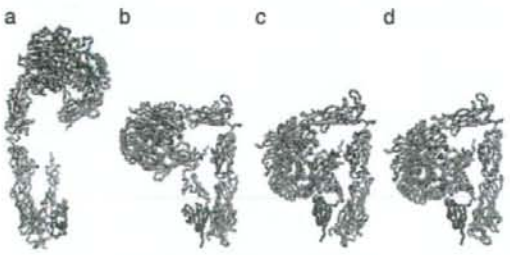

FIGURE 5 (*a–d*) Backbone structures of integrin at the end of iterative normal-mode calculations 1–4, respectively (Table 2).

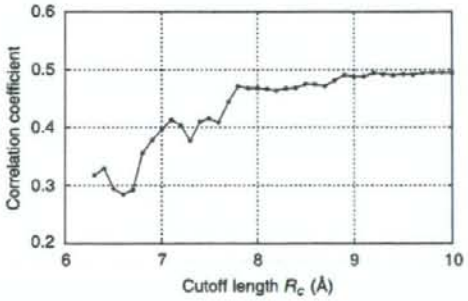

FIGURE 6 Correlation coefficient of the thermal atomic fluctuations derived from NMA and x-ray crystal structural data (B-factor) plotted against the cutoff length, R_c. Conventional elastic network models were used.